Batteries & Supercaps

Research Article
doi.org/10.1002/batt.202300092

Chemistry Europe
European Chemical Societies Publishing

www.batteries-supercaps.org

VIP *Very Important Paper*

Solvent-free Ternary Polymer Electrolytes with High Ionic Conductivity for Stable Sodium-based Batteries at Room Temperature

Daniel Roscher,[a, b] Yongil Kim,[a] Dominik Stepien,[a, b] Maider Zarrabeitia,*[a, b] and Stefano Passerini*[a, b, c]

Transitioning to solid-state batteries using polymer electrolytes results in inherently safer devices and can facilitate the use of sodium metal anodes enabling higher energy densities. In this work, solvent-free ternary polymer electrolytes based on cross-linked polyethylene oxide (PEO), sodium bis(fluorosulfonyl) imide (NaFSI) or sodium bis(trifluoromethanesulfonyl) imide (NaTFSI) and N-butyl-N-methyl-pyrrolidinium-based ionic liquids (ILs, $Pyr_{14}FSI$ or $Pyr_{14}TFSI$) are developed. Synthesized polymer membranes are thoroughly characterized, verifying their good thermal and electrochemical stability, as well as a low glass transition and crystallinity, thus high segmental mobility of the polymer matrix. The latter results in good ionic conductivities around 1×10^{-3} S cm^{-1} at 20 °C. The polymer electrolytes are successfully employed in sodium-metal battery (SMB) cells operating at room temperature (RT) and using P2-$Na_{2/3}Ni_{1/3}Mn_{2/3}O_2$ layered oxide as cathode. The electrochemical performance strongly depends on the choice of anion in the conducting sodium salt and plasticizing IL. Furthermore, this solid-state SMB approach mitigates capacity fading drivers for the P2-$Na_{2/3}Ni_{1/3}Mn_{2/3}O_2$, resulting in high Coulombic efficiency (99.91 %) and high capacity retention (99% after 100 cycles) with good specific capacity (140 mAh g^{-1}).

Introduction

Among the "beyond" lithium electrochemical energy storage systems, sodium-ion batteries (SIBs) are a promising technology, especially for large-scale stationary applications and light electromobility.[1] Implementing SIBs as an alternative or complement to the ubiquitous lithium-ion batteries (LIBs) offers the chance to reduce cost, improve sustainability and decrease the environmental impact of battery production.[2] Most state-of-the-art SIBs employ carbonate- or ether-based organic liquid electrolytes due to their high ionic conductivity, optimal viscosity, and satisfactory electrochemical performance.[1] However, for LIBs and SIBs, the use of conventional liquid electrolytes involves serious safety hazards owing to their high volatility, flammability, and risk of leakage. Side reactions between electrode and electrolyte, leaching of active material ions, and dendrite formation are additional issues detrimental to battery performance.[3] Due to their mechanical rigidity, solid electrolytes (SEs) may prevent dendrite growth during electrodeposition, enabling the use of sodium metal as anode and, thus, higher energy densities.[4] Although the jump in energy density for sodium-metal batteries (SMBs) is lower than for lithium-metal batteries (LMBs), future development will shift toward solid-state batteries (SSBs), which offer relevant advantages, especially enhanced battery safety.[3] SEs can inhibit unwanted "cross-talk" between the electrodes improving long-term cyclability and are more stable at elevated temperatures.[4] Besides the high energy density, they hold the potential to achieve high power density as well.[4,5]

SEs can be divided into two main classes, inorganic solid electrolytes (ISEs) and solid polymer electrolytes (SPEs). ISEs, which are crystalline, glassy, or glass-ceramic, possess high mechanical stability. Compared to SPEs, they usually feature higher ionic conductivities, especially at lower temperatures, as well as higher cation transference numbers. However, ISEs are still limited by their low thermodynamic stability, complex processability and interfacial contact issues.[4,6] Close contact at the solid-solid interface between electrodes and the SE is a key factor determining the electrochemical performance of SSBs.[6b] The softer SPEs excel due to their high flexibility. In addition, they can accommodate volume changes of electrode materials by elastic or plastic deformation and facilitate the formation or reconstruction of electrode-solid electrolyte interphases.[4,7]

The simplest form of SPEs is prepared by the dissolution of sodium salt/s in a polymer matrix, *e.g.*, polytrimethylene carbonate (PTMC), polymethyl methacrylate (PMMA) or polyethylene oxide (PEO). Electron withdrawing groups along the C–C polymer backbone complexing Na^+ ions enable the ion

[a] D. Roscher, Dr. Y. Kim, D. Stepien, Dr. M. Zarrabeitia, Prof. Dr. S. Passerini
Helmholtz Institute Ulm (HIU)
Helmholtzstrasse 11, 89081 Ulm (Germany)
E-mail: maider.ipina@kit.edu
stefano.passerini@kit.edu
[b] D. Roscher, D. Stepien, Dr. M. Zarrabeitia, Prof. Dr. S. Passerini
Karlsruhe Institute of Technology (KIT)
P.O. Box 3640, 76021 Karlsruhe (Germany)
[c] Prof. Dr. S. Passerini
Sapienza University of Rome
Chemistry Department
Piazzale A. Moro 5, 00185 Rome (Italy)

Supporting information for this article is available on the WWW under https://doi.org/10.1002/batt.202300092

pair dissociation and, therefore, the ion conduction mechanism is coupled to the intrinsic segmental mobility of polymer chains.[6a,c] Hence, the conductivity depends on the amorphicity of the polymer matrix when the chains are not locked in a crystal lattice. Many studies focus on PEO as an easily processable polymer capable of dissolving various sodium salts and exhibiting good compatibility with alkali metals.[6a,7,8] However, issues arise owing to the electrochemical instability at high voltages at which the electron-rich ether oxygen atoms readily oxidize.[6c] PEO:NaTFSI and PEO:NaFSI (EO/Na ratio of 20), for example, show good ionic conductivities around 1×10^{-3} S cm^{-1} and 4×10^{-4} S cm^{-1} at 80 °C, respectively.[8,9] For the latter, good interfacial stability with Na metal was reported, and polymer-based sodium-metal cells containing P2-$Na_{2/3}Ni_{1/3}Mn_{2/3}O_2$ or $Na_3V_2(PO_4)_3$ as cathode showed good cycling stability at 80 °C.[8] However, the RT conductivity of these SPEs is on the order of magnitude of 10^{-7} to 10^{-6} S cm^{-1},[8,10] which necessitates the battery operation at temperatures above the PEO melting point (60–70 °C). A high ionic conductivity at RT is crucial for developing practical solid-state sodium-batteries.[6b] In fact, while a RT conductivity of around 10^{-3} S cm^{-1} is sufficient on the lab scale, a conductivity $>10^{-2}$ S cm^{-1} is required to benefit from the use of SEs in practical applications.[5a,6b]

There are various physical and chemical approaches to enhance ionic conductivity.[6c] One method is through the addition of inorganic fillers, which can be inactive or Na^+-ion conducting, into SPEs. Combining polymers with inorganic materials increases mechanical strength and thermal stability and can facilitate increased salt dissociation in composite solid polymer electrolytes (CSPEs).[6c,9,11] Aside from the suppression of polymer crystallization, Na^+ ion transport paths on the surface of interconnected ISE particles and their bulk conduction can contribute to the increased conductivity.[6c,7,11] For a CSPE-based on polyvinylidene fluoride (PVDF), $NaClO_4$ and NASICON-type $Na_3Zr_2Si_2PO_{12}$, an ionic conductivity at RT (23 °C) as high as 1×10^{-4} S cm^{-1} was reported.[12] This significantly improved the cycling stability of Na|CSPE|$Na_{2/3}MnO_2$ cells, although a minimal amount of an organic liquid electrolyte had to be added for improved interface contact and compatibility. Nevertheless, CSPEs, just as dry SPEs at large, still fall short of the requirements for practical application, particularly at RT in terms of ionic conductivity, Na^+ ion transference number and interfacial stability.[7]

Another conventional approach to increase ionic conductivity is the incorporation of liquid plasticizers. The most prominent group are gel polymer electrolytes (GPEs), where the SPE is soaked in carbonate- or ether-based electrolytes due to their good ionic conductivity at RT (up to $\approx6\times10^{-3}$ S cm^{-1}). However, the mechanical stability is reduced, losing the solid-state nature and causing a setback in safety.[6a,7,13] Also, similar to conventional liquid electrolytes, GPEs suffer from severe decomposition of these types of solvents in contact with Na metal.[14] Albeit less favorable from a cost perspective, ILs with melting points below RT are interesting plasticizers due to their non-flammable properties, very low vapor pressure, and superior electrochemical and thermal stability.[14] This idea was first implemented in 1996 by the group of Watanabe for Li^+ ion conducting polymers,[16] taken up again in 2003,[17] and further explored until now.[15b] Since solid-state sodium-based batteries are still in their infancy, a limited number of publications are available on Na^+ ion conducting analogues, and even less demonstrating their application (at RT) in prototype cells.[7] Boschin and Johansson studied PEO:NaTFSI and PEO:NaFSI SPEs with different compositions plasticized by N-methyl-N-propyl-pyrrolidinium-based ILs, Pyr_{13}TFSI or Pyr_{13}FSI, with moderate contents up to 20 wt.%. TFSI-based SPE with 20 wt.% IL (EO:Na:IL molar ratio ≈20:2:1) showed the highest ionic conductivity of around 1×10^{-4} S cm^{-1} at 30 °C.[18] From research on SPEs for lithium-based systems,[6c,19] it is known that cross-linking reduces the crystallinity of the polymer matrix while enhancing mechanical properties and for those ternary SPEs facilitates higher plasticizer contents without losing the solid-state configuration, thus even higher conductivities at RT.[19] Rani *et al.* prepared a ternary polymer electrolyte using polyvinyl chloride, NaFSI and 1-ethyl-3-methylimidazolium FSI (Im_{12}FSI) IL (50 wt.%), which showed a good ionic conductivity of 1.7×10^{-3} S cm^{-1} at RT. They reported the first 5 cycles of a polymer-based SMB cell, employing $Na_2FeP_2O_7$ as cathode, operated at 90 °C, reaching a reversible capacity of 92 mAh g^{-1} and a Coulombic efficiency of 97.3% in the 5th cycle. Fdz De Anastro *et al.* presented self-standing membranes based on poly(dimethyldiallylammonium)-TFSI belonging to the special polymer class of poly(ionic liquids) as host for NaFSI and Pyr_{13}FSI.[21] The addition of alumina nanoparticles enhanced the mechanical properties. The poly(ionic liquid) incorporating 50 wt.% of IL and 5 wt.% Al_2O_3 reached an ionic conductivity around 1×10^{-4} S cm^{-1} at 30 °C and Na|poly(ionic liquid)|$NaFePO_4$ cells achieved an initial capacity of 114 mAh g^{-1} at 0.05 C with a Coulombic efficiency >97% and a capacity retention of around 78% after 60 cycles at 70 °C. Our group recently demonstrated the applicability of a ternary SPE comprising cross-linked PEO, NaFSI and the N-butyl-N-methyl-pyrrolidinium IL Pyr_{14}FSI (63 wt.%) combined with a NASICON ($Na_3Zr_2Si_2PO_{12}$) ISE in a layered composite in anode-less sodium seawater batteries at 20 °C for power to metal/metal to power energy storage.[22]

In this work, solvent-free ternary polymer electrolytes based on PEO, sodium salts (NaFSI or NaTFSI) and N-butyl-N-methyl-pyrrolidinium ILs (Pyr_{14}FSI or Pyr_{14}TFSI) were investigated to replace the conventional non-aqueous liquid electrolyte in sodium-based batteries. A high IL plasticizer content is expected to achieve a good RT ionic conductivity while cross-linking of the polymer chains is utilized to maintain mechanical stability. Synthesized SPE membranes have been thoroughly characterized by a set of thermal and electrochemical analysis techniques to study the thermal and electrochemical stability, as well as thermal transitions and crystallinity. Electrochemical impedance spectroscopy (EIS) has been applied to determine the temperature dependent ionic conductivity and unravel the compatibility of the polymer|Na metal interface. The performance of the SPE membranes was tested in SMB cells operating at RT using the P2-$Na_{2/3}Ni_{1/3}Mn_{2/3}O_2$ (henceforth NM) layered oxide as cathode material.

Research Article
doi.org/10.1002/batt.202300092
Chemistry Europe
European Chemical Societies Publishing

Results and Discussion

NM cathode material physicochemical characterization

The elementary analysis by inductively coupled plasma optical emission spectrometry (ICP-OES) yields a metal stoichiometry of $Na_{0.65}Ni_{0.33}Mn_{0.67}O_2$, confirming the targeted stoichiometry of the cathode material. The structural properties of the NM layered oxide have been determined by X-ray diffraction (XRD) analysis. Rietveld refinement of the XRD powder pattern reported in Figure 1(a) reveals that NM belongs to the P2-type structure and crystallizes in the hexagonal $P6_3/mmc$ space group with MO_2 slabs having an ABBA stacking arrangement. Na^+ ions occupy prismatic sites sharing either faces or edges with the MO_6 octahedrons of adjacent sheets (Table S1 and unit cell in the inset of Figure 1a). However, a minor contribution of a cubic NiO impurity was found (Figure S1).

Scanning electron microscopy (SEM) has been carried out to investigate the morphology of the NM cathode material and electrodes. SEM micrographs reported in Figure 1(b–e) show that NM particles exhibit a flake-like morphology with a primary particle size ranging from 1 to 7 μm (Figure 1b). The defined layered structure of this material is observable at higher magnification (Figure 1c). At the electrode level (Figure 1d and e), the NM platelets are oriented parallel to the electrode surface in large part, however, tilts and gaps not filled by the spherical conductive carbon additive create a micro surface roughness on the scale of the NM primary particle size.

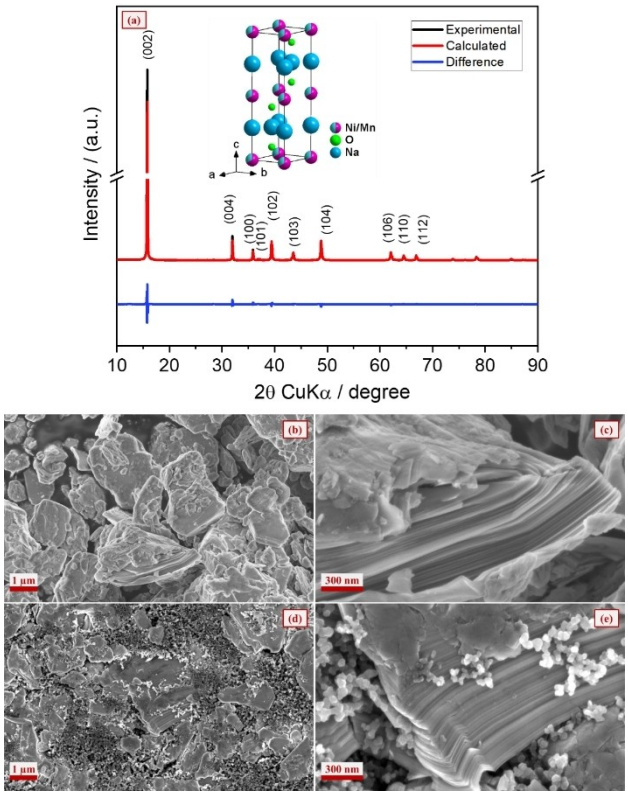

Figure 1. a) Results of the Rietveld refinement on a powder XRD pattern of $Na_{2/3}Ni_{1/3}Mn_{2/3}O_2$ (NM – structural parameters are listed in Table S1, inset reports a schematic illustration of the unit cell) and SEM micrographs at various magnifications of b, c) the NM material in the pristine powder state and (d, e) the NM electrode.

SPE thermal and electrochemical characterization

Four different chemical compositions of SPE membranes were prepared, which are composed of PEO, sodium salt (NaFSI or NaTFSI) and IL ($Pyr_{14}FSI$ or $Pyr_{14}TFSI$). Fluorine-containing anions were chosen as fluorine is known to form stable electrode-electrolyte interfaces upon cycling of lithium- and sodium-batteries *via* the formation of inorganic, fluoride-rich interphases (LiF or NaF).[23–26] Furthermore, comparable fluorine-containing polymer electrolytes have already been studied for lithium-based batteries with good electrochemical performance.[27] In contrast, for sodium-based batteries, poorer electrochemical performances were reported at RT due to the low amount of plasticizer and the absence of PEO cross-linking.[18] The investigated four different formulations have been selected to understand the influence of the fluorine concentration. Exchanging the anion in either the salt or the IL is an easy approach to vary the molar ratio of FSI and TFSI and study its implication on the SPE properties and performance of sodium-metal polymer battery cells. Indeed, it was observed that the mix of FSI and TFSI anions is favorable for lithium-based batteries.[28] Synthesized samples are termed by the salt anion followed by the IL anion, *e.g.*, the SPE comprising PEO, NaTFSI and $Pyr_{14}FSI$ is referred to as TFSI:FSI (Table 1).

The self-standing cross-linked ternary SPE membranes depicted in Figure 2(a) are flexible, stretchable, and strongly adhesive. The latter is specifically beneficial for good contact to preferably plain electrodes. However, a small amount of contact solution was applied at interfaces to ease the handling by reducing self-adhesion and to promote the adaption to electrodes exhibiting surface roughness and porosity. A mixture of Na salt and IL in a 1:4 molar ratio, as incorporated in the SPE, was

Table 1. Decomposition temperature (T_d, determined from Figure 2b), glass transition temperature (T_g, determined from Figure 2d), equilibrium glass transition temperature (T_0), pseudo activation energy (B) for ion conduction in the SPE bulk and ionic conductivity at 20 °C (σ (20 °C), determined together with T_0 and B from Figure 3a) of all four synthesized SPEs.

SPE label	Polymer	Salt	IL	T_d [°C]	T_g [°C]	T_0 [°C]	B [eV]	σ (20 °C) [10^{-3} S cm^{-1}]
FSI:FSI	PEO	NaFSI	$Pyr_{14}FSI$	250	−87	−93	0.06	1.2
TFSI:FSI	PEO	NaTFSI	$Pyr_{14}FSI$	258	−84	−92	0.06	1.1
FSI:TFSI	PEO	NaFSI	$Pyr_{14}TFSI$	258	−76	−90	0.06	0.8
TFSI:TFSI	PEO	NaTFSI	$Pyr_{14}TFSI$	350	−72	−80	0.06	0.7

Research Article
doi.org/10.1002/batt.202300092
Chemistry Europe
European Chemical Societies Publishing

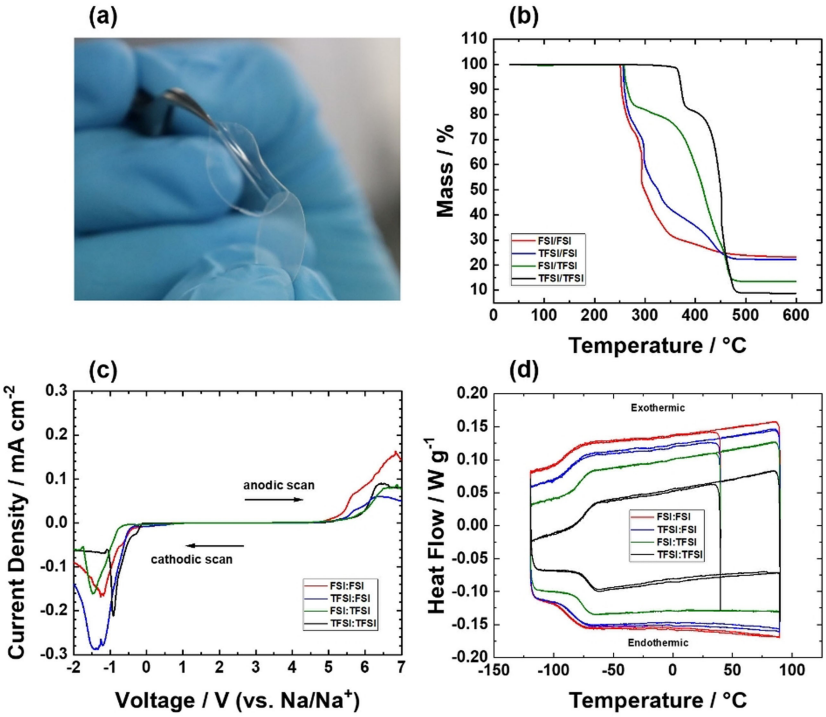

Figure 2. a) Photograph of the FSI:FSI SPE, b) TGA curves (heating rate of 5 K min^{-1}, inert N_2 atmosphere), c) anodic and cathodic LSV curves (Al foil as working electrode, Na metal as counter and reference electrode, scan rate of 0.1 mV s^{-1}) and d) DSC curves (two cooling and heating cycles between −120 °C and 90 °C, cooling/heating rate of 5 K min^{-1}, 30 min isothermal holds at the turning points) of all four synthesized SPEs.

used. Presumably, this is later consumed in the electrode-electrolyte interphase formation on both sides, fills the cathode porosity and/or is absorbed by the SPE, as no liquid residue was found after disassembling cycled cells (Figure S2).

The thermogravimetric analysis (TGA) curves reported in Figure 2(b) evidence the high thermal stability of the SPEs. The first loss in weight occurring for the least stable purely FSI-based polymer (FSI:FSI) around 250 °C corresponds to the decomposition of the PEO matrix. The onset of decomposition of the other two FSI-containing polymers, *i.e.*, TFSI:FSI and FSI:TFSI, is only slightly higher at around 258 °C. The purely TFSI-based SPE (TFSI:TFSI) is the most stable membrane exhibiting a PEO decomposition onset around 350 °C. The FSI anion, regardless of if introduced by the salt or IL, reduces the SPE's thermal stability due to its lower thermal stability and higher reactivity compared to the TFSI one, which was reported for similar Li SPEs.[27] NaFSI already starts to decompose at temperatures above 125 °C.[29] Huang and Hollenkamp proposed a decomposition mechanism for LiFSI in the absence of water,[30] which can probably be applied to NaFSI. They suggested that heating possibly promotes breaking of the S–N bond in the FSI anion. The forming radicals may initiate the PEO decomposition at lower temperatures. In the presence of NaTFSI and Pyr_{14}FSI, the formation of NaFSI by ion exchange can be expected. For the Pyr_{14}FSI-based polymers (FSI:FSI and TFSI:FSI), PEO decomposition is directly followed by the decomposition of the Na salt/IL mixture around 280 °C as known from the decomposition behavior of comparable IL-based electrolytes reported in the literature.[31] Due to the known higher thermal stability of the TFSI anion,[29] the Na salt/IL decomposition is progressively delayed to higher temperatures with increasing TFSI content.

To study the electrochemical stability of the SPEs, linear sweep voltammetry (LSV) was performed. The anodic and cathodic scans are reported in Figure 2(c). In the cathodic sweep, no significant current densities indicating a reduction of the SPEs are measured before Na plating below 0 V. Based on a threshold current density of 10 μA cm^{-2}, the apparent oxidation (anodic) stability potential limit increases from 5.1 V for FSI:FSI to 5.4 V for TFSI:FSI, and 5.5 V for FSI:TFSI and TFSI:TFSI. These thresholds, taken using flat electrodes, contradict the literature which commonly reports an anodic stability limit of 3.8 V vs. Li/Li$^+$ (corresponding to 3.5 V vs. Na/Na$^+$) for PEO polymers,[32] as well as our experience with built SMB cells. When cycled within the full voltage range of the NM cathode material from 4.3 to 1.5 V, unstable cycling behavior is observed with prolonged charge profiles at potentials above 3.8 V (see Figure S3), most likely due to PEO oxidation resulting in the decomposition of the SPE. Nevertheless, stable cycling is achieved when the voltage range is restricted to an upper cut-off voltage of 3.8 V (see below).

Differential scanning calorimetry (DSC) was applied to disclose thermal transitions occurring within the SPEs. The lack of melting/crystallization peaks in the thermograms shown in Figure 2(d) indicates that all SPEs are fully amorphous. The step-like features occur due to the glass transition (T_g), which increases in the following order FSI:FSI < TFSI:FSI < FSI:TFSI < TFSI:TFSI (see Table 1). The low T_g and crystallinity imply high

segmental mobility of the polymer matrix. This results mainly from the high IL content (63–72 wt.%) incorporated in the SPEs acting as plasticizer. The cross-linking is another factor in ensuring low crystallinity while at the same time improving mechanical stability.[19]

The ionic conductivity of the SPEs as a function of temperature in a range of 10 to 90 °C is reported in Figure 3(a). According to the trend in T_g, the conductivity decreases in the order FSI:FSI > TFSI:FSI > FSI:TFSI > TFSI:TFSI, *i.e.*, the purely FSI-based SPE (FSI:FSI) with the lowest T_g, offering the highest segmental mobility of the PEO matrix, exhibits the highest conductivity at all temperatures measured. Nevertheless, a good ionic conductivity around 1×10^{-3} S cm^{-1} is already reached at 20 °C for all SPEs, the precise values are listed in Table 1. For FSI:FSI, the tabulated value is in good agreement with previous work.[22] The thermal reversibility has been investigated by ramping down the temperature after ramping up. The conductivities determined in the forward and backward scans coincide (Figure S4), showing excellent thermal reversibility of all SPEs.

The ionic conductivity of SPEs increases to about 1×10^{-2} S cm^{-1} at 90 °C displaying the typical Vogel-Tammann-Fulcher (VTF) behavior as indicated by the curvature. The empirical derived VTF equation shown as an inset in Figure 3(b) can be applied to fit the data points to retrieve parameters like the equilibrium glass transition temperature (T_0) and the pseudo activation energy (B). T_0 is introduced to consider that the measured T_g is kinetically influenced by the heating/cooling rate and represents the temperature below which segmental motion is fully restrained when the heating/cooling rate is infinitesimally low. As expected, T_0 shows the same trend (Figure S5) as measured T_g (see Table 1), confirming that the segmental mobility decreases with increasing TFSI content. B is the counterpart to the activation energy E_a in the Arrhenius equation. It can be used to measure the energy barrier for the conduction of ions, including Na^+ ions, within the bulk to compare the different SPEs. As depicted in Figure 3(b), B reaches the same value of about 0.06 eV for all SPEs, which is in good agreement with a value reported for FSI:FSI.[22] This implies that, in our case, the segmental mobility of the polymer matrix, represented by T_g, is the fundamental driver of differences in ionic conductivity.

SPE | Na interface

The direct characterization of the SPE | Na interface is impeded as the individual cell components are fused together after cycling due to the high adhesivity of the polymer electrolyte. As a matter of fact, this is an important characteristic of well-performing SPE-based cells but makes it impossible to separate the cell components and perform post-mortem analysis. Therefore, the SPE | Na interface was studied by EIS of symmetric Na | SPE | Na cells at open circuit before and after cycling. To emphasize the differences between the FSI and TFSI anions, we focus on the single anion SPEs (*i.e.*, FSI:FSI and TFSI:TFSI). The Nyquist plots in Figure 4(a and c) show an unambiguous difference in the impedance response of FSI:FSI and TFSI:TFSI SPEs. The equivalent circuit (see inset of Figure 4a) to fit the experimental data of FSI:FSI cells consists of a resistor for the bulk resistance (R_b, due to the electrolyte and cell parts) and two *RC* elements. Due to non-ideal capacitances indicated by depressed semicircles, capacitors (C_s) were replaced by constant phase elements (CPEs). After the initial EIS measurement (t = 0 h), the first *RC* element includes a Warburg element (W with Warburg coefficient A_W), suggesting that the Na^+ ion diffusion is a limiting process. The first *RC* element is attributed to the charge transfer resistance (R_{CT}) and the double layer capacitance (CPE_{DL}) at the Na metal surface. In addition, the contribution of the solid-electrolyte interphase (SEI) cannot be disregarded, therefore, the SEI resistance (R_{SEI}) must be included in R_{CT}. The second *RC* element is attributed to the ion transfer into the SPE bulk membrane (R_M and CPE_M). For TFSI:TFSI cells, an additional *RC* element (inset of Figure 4c) is needed to model the impedance data, which is attributed to the formation of a passivating SEI on the Na metal (R_{SEI} and CPE_{SEI}). In Na | FSI:FSI | Na cells, the contribution of the SEI to the impedance is presumably low compared to the charge transfer

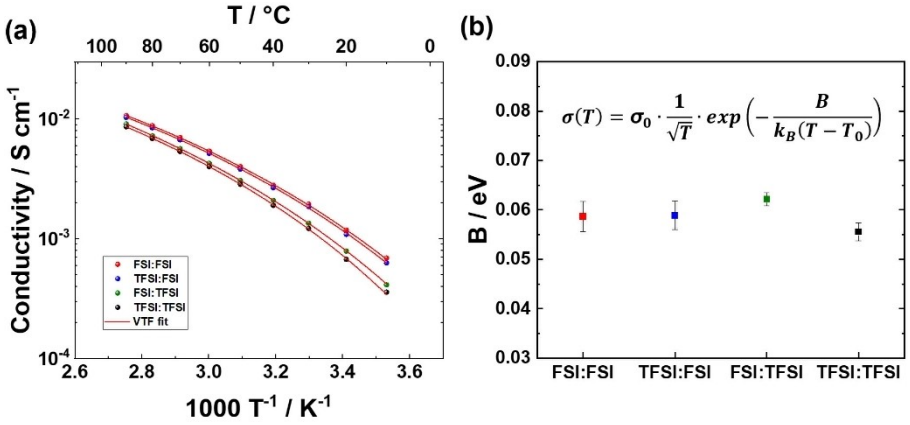

Figure 3. a) Temperature-dependent ionic conductivity and Vogel-Tammann-Fulcher (VTF) fit and b) pseudo activation energy (B) for ion conduction in the SPE bulk determined by the fit for all four synthesized SPEs.

Research Article
doi.org/10.1002/batt.202300092
Chemistry Europe
European Chemical Societies Publishing

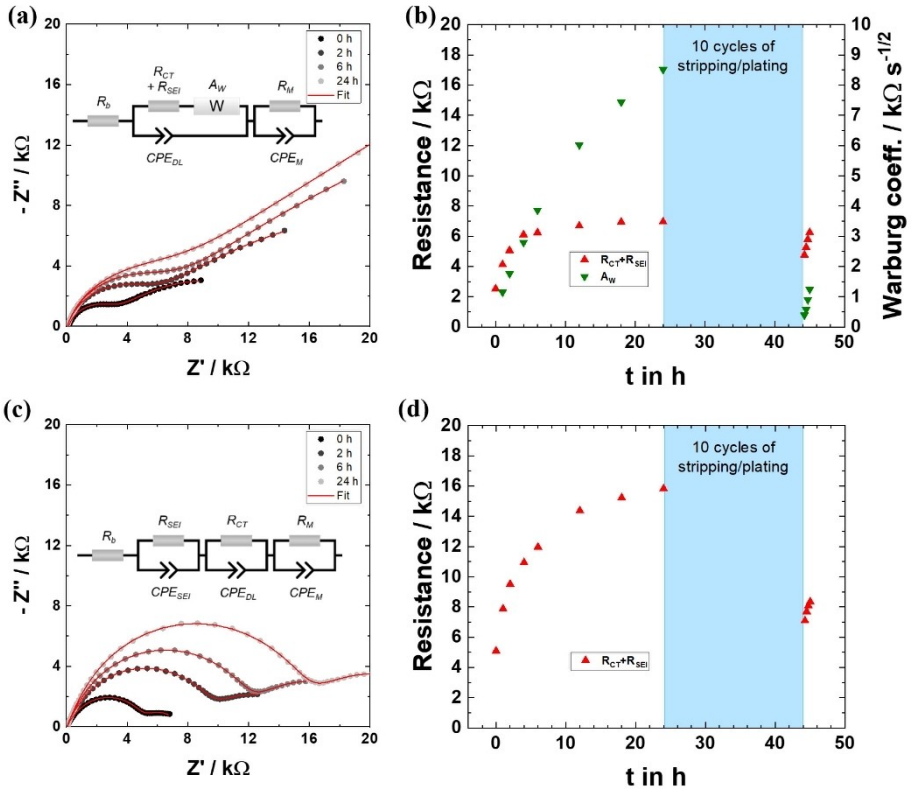

Figure 4. Nyquist plots collected from the electrochemical impedance spectra of the symmetric a) Na|FSI:FSI|Na and c) Na|TFSI:TFSI|Na cells resting at OCV for 24 h (temperature 20 °C ± 2 °C). The equivalent circuits to fit the data are shown as inset, respectively. Results of the equivalent circuit fitting for the symmetric b) Na|FSI:FSI|Na and d) Na|TFSI:TFSI|Na cells.

(CT) and/or both processes (SEI and CT) exhibit similar time constants, making it impossible to differentiate them. Furthermore, in the TFSI:TFSI cells, the Warburg element doesn't apply, suggesting that the Na^+ ion diffusion is not a limiting factor. The results of the equivalent circuit fitting are reported in Figure 4(b and d).

In the Na|FSI:FSI|Na cell, $R_{CT}+R_{SEI}$ (Figure 4b, red) increases almost linearly at first, which may be caused by the growing SEI, but the slope decreases after 6 h of rest and $R_{CT}+R_{SEI}$ stabilizes at around 7 kΩ. This suggests that after 6 h, the SEI has stabilized due to the decomposition of the electrochemically less stable FSI anion, forming a beneficial fluorine-rich interphase.[23] A_W increases continuously within 24 h at OCV. The real and imaginary part of the impedance of a Warburg element are linearly dependent on A_W. For a simple redox reaction at an electrode, the coefficient itself depends on the surface area A, the diffusion coefficients D_O and D_R and the bulk concentrations $c_{O,b}$ and $c_{R,b}$ of the oxidized and reduced species, respectively, according to Equation (1).[33]

$$A_W = \frac{RT}{n^2F^2A\sqrt{2}}\left(\frac{1}{c_{O,b}\sqrt{D_O}}+\frac{1}{c_{R,b}\sqrt{D_R}}\right) \quad (1)$$

For the stripping/plating reaction ($n=1$), the last summand is irrelevant since the Na metal is an insoluble solid and Equation (1) simplifies to:

$$A_W = \frac{RT}{F^2Ac_{Na^+,b}\sqrt{2D_{Na^+}}} \quad (2)$$

According to Equation (2), A_W is inversely proportional to surface area (A), and the bulk concentration $c_{Na^+,b}$ and square root of the diffusion coefficient D_{Na^+} of Na^+ ions. That the surface area (A) of the Na electrodes decreases during rest at OCV is not expected. The increase in A_W must thereby derive from a decline in $c_{Na^+,b}$ and D_{Na^+}. This can be explained by absorption of the salt/IL contact solution by the polymer membrane and possibly its incremental spread to the interface by polymer creep. After ten cycles of stripping (1 h) and plating (1 h), A_W is reduced from about 8.5 kΩ $s^{-1/2}$ to 0.4 kΩ $s^{-1/2}$, which results from a more than 20-fold (10-fold per Na electrode) increase in surface area as a corresponding increase in $c_{Na^+,b}$ or D_{Na^+} is unreasonable. Hence, the FSI:FSI SPE is able to maintain a good contact despite the high surface area enlargement. Within 1 h, A_W is increasing again to about 1.2 kΩ $s^{-1/2}$ indicating a 3-fold decrease in surface area, i.e., the polymer provides enough mechanical stability to facilitate the partial compression of deposited Na. The $R_{CT}+R_{SEI}$ decreases only by about one-third and converges toward its value before stripping/plating reaching 6.2 kΩ after 1 h. Normalized to the surface area, this implies an increase in $R_{CT}+R_{SEI}$, which indicates for the reconstruction of the SEI after the Na metal stripping/plating, *i.e.*, the SEI shows a dynamic behavior even upon open circuit conditions.

Research Article
doi.org/10.1002/batt.202300092
Chemistry Europe
European Chemical Societies Publishing

In contrast, $R_{CT}+R_{SEI}$ in the TFSI:TFSI polymer cell (Figure 4d) doesn't stabilize within 24 h rest at OCV reaching a value of 15.8 kΩ. Compared to the FSI:FSI cell, $R_{CT}+R_{SEI}$ is more than twice as high at least after 24 h. This indicates that the SEI is unstable, still forming after 24 h, probably because the TFSI anion is electrochemically more stable, as indicated above, thus not forming a fluoride-rich and stable interphase. After stripping and plating, $R_{CT}+R_{SEI}$ is again higher than its counterpart in the FSI:FSI cell, indicating poorer interfacial compatibility between the SPE membrane and the Na metal. In total, the resistance of the Na|TFSI:TFSI|Na cell is nearly twice as high as its FSI:FSI-based analogue, which will affect the electrochemical performance (shown below).

Sodium-metal polymer battery testing

To evaluate the practicality and performance of synthesized SPEs at ambient temperature, sodium-metal polymer battery cells were assembled. NM (P2-$Na_{2/3}Ni_{1/3}Mn_{2/3}O_2$) was used as a representative of layered transition metal oxide cathode materials. Its electrochemical behavior in the organic liquid electrolyte is characterized by several structural changes upon cycling, from a P2-type structure to a biphasic P2- and O2-type stacking, when the sodium amount is lower than 1/3, as indicated by the stepped charge and discharge profiles shown in Figure S6.[34] NM exhibits a theoretical capacity of 173 mAh g^{-1} ($^2/_3$ equivalent of Na). Still, in the full voltage range from 4.3 to 1.5 V, 0.84 equivalents of Na, which is close to the maximum sodium content ($\leq$0.85) for P2-type layered oxides,[35] can be stored in the material. Due to the degradation of the SPE at higher potentials, the upper cut-off voltage was limited to 3.8 V. This conveniently excludes the P2-O2 phase transition occurring at potentials above 4.2 V, which causes rapid capacity fading.[36] The remaining major processes associated with material degradation are the instability of the cathode electrolyte interphase (CEI) and the formation of Jahn-Teller active Mn^{3+} below 2 V, which can lead to manganese dissolution.[35,37]

The voltage profiles of the 5th and 50th cycle for the cells with the FSI:FSI and TFSI:FSI SPE membrane formulations using NM as cathode and Na metal as anode are summarized in Figure 5, while those of FSI:TFSI and TFSI:TFSI are shown in Figure S7. For comparison, the voltage profile in the carbonate-based liquid electrolyte is included (the direct comparison is given in Figure S8). Even though the SPEs exhibit very similar thermal and electrochemical properties, the NM's electrochemical performance highly depends on the choice of conducting salt and plasticizing IL anion in the SPE. All polymer-based cells exhibit polarization compared to the carbonate-based liquid electrolyte cell, which could be one of the reasons for the lower delivered specific capacity. The polarization is increasing in the following order FSI:FSI < TFSI:FSI < FSI:TFSI < TFSI:TFSI. This agrees with the impedance measurements on symmetric

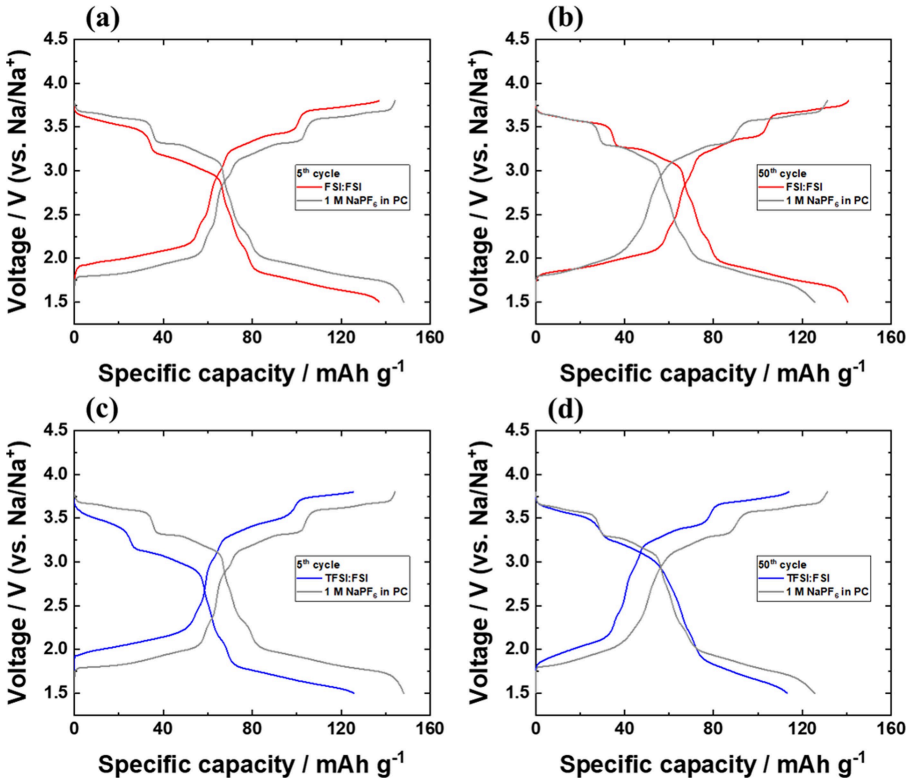

Figure 5. Voltage profiles of a, b) the FSI:FSI-based and c, d) TFSI:FSI-based SMB cell using NM as cathode in the 5th and 50th cycle (galvanostatic cycling with a current of 17 mA g^{-1} between 3.8 V and 1.5 V, temperature 20 °C ± 2 °C). For comparison, the voltage profile in the carbonate-based liquid electrolyte is included.

Research Article
doi.org/10.1002/batt.202300092
Chemistry Europe
European Chemical Societies Publishing

Na|SPE|Na cells, which revealed higher resistances in the TFSI-containing SPE cell. For the purely FSI-based SPE (FSI:FSI, Figure 5a and b), the cell polarization decreases upon cycling until the level of the liquid electrolyte cell is reached, as evident when comparing the 5th with the 50th cycle. Among studied SPE-based cells, Na|FSI:FSI|NM shows the lowest polarization and delivers the highest specific capacity. In addition, it is observed that the SPE successfully suppresses manganese dissolution (voltage plateau at 1.7–1.8 V in Figure 5a and b). The capacity associated with the manganese redox plateau in the 5th cycle (55 mAh g^{-1}) is even slightly increased in the 50th cycle (58 mAh g^{-1}) due to the decreased cell polarization. In contrast, the cell operating with carbonate-based liquid electrolyte loses about a third of the manganese redox capacity after 50 cycles (5th cycle: 60 mAh g^{-1}, 50th cycle: 40 mAh g^{-1}). Therefore, as confirmed below, the capacity retention is expected to be enhanced using the SPE. The Pyr_{14}FSI-based polymer containing NaTFSI as conducting salt (TFSI:FSI, Figure 5c and d) shows larger polarization, but similar behavior as FSI:FSI in the initial cycles, leading to a similar specific capacity. For the Pyr_{14}TFSI-based polymer electrolytes (FSI:TFSI and TFSI:TFSI), the polarization in the cell is increasing upon cycling (Figure S7a and b) and eventually drives the specific capacity to practically zero. Hence, it becomes apparent that the TFSI anion, although more thermally and electrochemically stable than the FSI anion, has a detrimental effect on the performance of the polymer-based SMB cells using NM as a cathode.

The long-term stability of NM in FSI:FSI, TFSI:FSI and carbonate-based liquid electrolyte SMB cells is illustrated in Figure 6. After the initiation phase, during which good contact of the SPE to the electrodes is probably built, reducing the overall cell resistances, the cell comprising FSI:FSI reaches a specific capacity of 140 mAh g^{-1} in the 10th cycle. After 100 cycles, the cell exhibits outstanding capacity retention of 99% and a very stable Coulombic efficiency of 99.91% on average. The excellent Coulombic efficiency delivered might be related to the fact that the FSI anion forms a more beneficial SEI due to its lower stability, as indicated by the EIS results. The

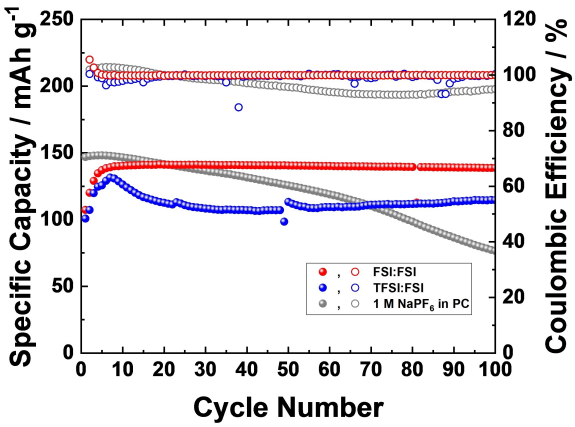

Figure 6. Reversible capacity (filled circle) and Coulombic efficiency (unfilled circle) of the Na|FSI:FSI|NM, Na|TFSI:FSI|NM and Na|1 M $NaPF_6$ in PC|NM cell (galvanostatic cycling) with a current of 17 mA g^{-1} between 3.8 V and 1.5 V over 100 cycles (temperature 20 °C ± 2 °C).

TFSI:FSI cell reaches a maximum specific capacity of 131 mAh g^{-1} in the 7th cycle and still achieves good capacity retention of 87%. The Coulombic efficiency is less stable than for FSI:FSI but averages 99.3% due to the presence of TFSI anions. Meanwhile, the FSI:TFSI and TFSI:TFSI cells exhibit insufficient capacity, or even no capacity (Figure S9a) due to severe polarization and the unstable Coulombic efficiency, which suggest poor SEI formation properties (note that the TFSI concentration is higher in the mentioned SPEs). This is also observed by EIS, and/or a low Na^+ ion transference number as reported for TFSI-containing SPEs for solid-state Li batteries.[38] Conversely, the cell with the conventional liquid electrolyte, 1 M $NaPF_6$ in PC, displays poor capacity retention of 52% after 100 cycles and an unstable and low Coulombic efficiency affected adversely by the Na metal counter electrode, which is known to exacerbate irreversible side reactions in organic carbonate-based electrolytes,[14] and the phase degradation due to the manganese dissolution upon cycling.[37]

To demonstrate that the excellent and poor cycling performance of the FSI:FSI and TFSI:TFSI SPE, respectively, is not the result of the contact solution on its own, the Na salt/IL mixtures were solely employed as electrolyte (i.e., NaFSI in Pyr_{14}FSI and NaTFSI in Pyr_{14}TFSI with a 1:4 molar ratio, respectively, Figure S9b). The cells do not show the initiation phase that occurs for the SPEs. Although they exhibit a high and stable Coulombic efficiency, after stable cycling for 30 cycles, capacity fading is observed, resulting in capacity retention of only 74% and 75%, respectively. This verifies that the SPE governs the cycling performance of the SMB cells and not the added IL solution.

Therefore, the high capacity retention and Coulombic efficiency of the Na|FSI:FSI|NM SMB cell prove the formation of a stable CEI. As a result, although the NM cell containing FSI:FSI electrolyte initially delivers a lower specific capacity than the cell containing carbonate-based liquid electrolyte, the SPE-based cell outperforms the liquid-based cell after 30 cycles due to superior capacity retention and Coulombic efficiency, which results in an energy density of 310 Wh kg^{-1} (NM and theoretical Na weight).

Conclusions

In this work, solvent-free ternary SPEs based on PEO, Na salts and ILs were developed, which offer promising properties for application in sodium-based batteries. The synthesis process is completely solvent-free, allowing easy upscaling. The extensive characterization revealed good thermal and electrochemical stability up to 3.8 V, as well as high amorphicity and low glass transition temperatures, thus, high segmental mobility of the polymer matrix. The latter results in good ionic conductivities around 1×10^{-3} S cm^{-1} already at 20 °C. The electrochemical performance of SMB polymer cells operated at ambient temperature strongly depends on the anion included in the conducting salt and plasticizing IL. The TFSI anion causes a high and increasing polarization in the cells upon cycling, as well as poor SEI formation, rendering them inoperable. On the

other hand, cells comprising the purely FSI-based SPE reach specific capacities of 140 mAh g^{-1} and exhibit a very stable average Coulombic efficiency of 99.91 % and capacity retention of 99 % after 100 cycles. This is an outstanding performance especially compared to the conventional carbonate-based liquid electrolyte. Hence, this solid-state approach can overcome the drivers of capacity fading for the layered P2-$Na_{2/3}Ni_{1/3}Mn_{2/3}O_2$ used as cathode material such as the instability of the cathode-electrolyte interphase and manganese dissolution. Despite these advances, further study is necessary to gain insight into the processes occurring at the electrode interfaces and to improve the polymer matrix to facilitate higher anodic as well as mechanical stability. However, the superior cycling stability and high Coulombic efficiency observed with a purely FSI-based solid-state electrolyte suggests that alternative and safer electrolytes should be developed to replace the standard carbonate-based liquid electrolytes for sodium-based technology.

Experimental Section/Methods

Cathode material synthesis and electrode preparation. A P2-type layered oxide with nominal composition $Na_{2/3}Ni_{1/3}Mn_{2/3}O_2$ was prepared by co-precipitation followed by a solid-state reaction as described previously.[39] Briefly, stoichiometric amounts of $NiSO_4 \cdot 6H_2O$ (Sigma Aldrich, ACS reagent, 99 %) and $MnSO_4 \cdot H_2O$ (Sigma Aldrich, puriss. p.a., 99.0–101.0 %) were dissolved in water, and an aqueous solution of NaOH (50 % excess) was added dropwise under an inert Ar atmosphere. The precipitated hydroxide precursor $Ni_{1/3}Mn_{2/3}(OH)_2$ was filtered, washed, and dried overnight. For the subsequent solid-state reaction, the precursor was mixed with 0.685 equivalents of NaOH (Sigma Aldrich, reagent grade $\geq$98 %, pellets were ground prior to use). The powder mixture was pelletized and annealed in air first at 500 °C for 5 h, then at 900 °C for 6 h, allowing the material to cool down to RT slowly. The obtained NM material was ground and sieved (< 45 μm).

The NM electrodes were prepared by dispersing the active material (85 wt.%), Super C65 conductive carbon black (IMERYS, 10 wt.%) and polyvinylidene-di-fluoride binder (PVDF, Solvay, Solef® 6020, 5 wt.%) in N-methyl-2-pyrrolidone (NMP, Sigma-Aldrich 99.5 %, anhydrous). The mixture was ball milled for 2 h in a zirconia jar (1 h milling, 10 min rest, 1 repetition, main disc speed 400 rpm, rotating plates speed 800 rpm). The obtained slurry was cast on Al foil (15 μm thickness, battery grade) using a doctor-blade (height 100 μm) and dried at 80 °C. Electrodes with 12 mm diameter were punched out, dried at 120 °C under vacuum, pressed with a constant load of 78.5 kN, and dried again at 120 °C under vacuum for 12 h. The mass loading of the electrodes was ~2.0 mg cm^{-2} (1.7 mg cm^{-2} active material, electrode thickness of 24 μm). NM electrodes were stored in an Ar-filled glove box (MB200B ECO, MBraun) with a H_2O and O_2 content lower than 0.1 ppm.

Polymer electrolyte synthesis. The SPE membranes were prepared in a dry room (dew point < −60 °C at 20 °C) according to literature.[22,40] Prior to use, all chemicals were dried under vacuum using a mechanical pump and a turbomolecular pump, subsequently, as specified previously.[22,31] PEO (Dow Chemical, WSR 301, M_w = 4 000 000) and sodium salt were mixed in a glass beaker. A solution of benzophenone (BP, Sigma Aldrich, ≥99.0 %), used as a cross-linking agent, in IL was added to obtain an ethylene oxide (EO) : Na : IL molar ratio of 10 : 1 : 4 and a BP/PEO mass ratio of 5 %. After thorough mixing, the resulting gum-like material was sealed under vacuum in a pouch bag and annealed at 100 °C overnight. The transparent and homogeneous compound was hot pressed at 100 °C with a final pressure of 15 bar and the obtained SPE film (thickness ~150 μm) was cross-linked by UV light irradiation (Cube photo-irradiator, 350 W Hg lamp) for 3 min on either side. NaFSI (Solvionic, 99.9 %) or NaTFSI (Solvionic, 99.5 %) and $Pyr_{14}FSI$ or $Pyr_{14}TFSI$, synthesized in-house according to Montanino et al.,[41] were used as conducting sodium salt and plasticizing IL, respectively.

Material characterization. The elemental composition of the prepared NM material was determined by ICP-OES on a Spectro Arcos spectrometer (Spectro Analytical Instruments). The structural properties were analysed by powder XRD using Cu Kα radiation (λ = 0.154 nm) of a Bruker D8 Advance diffractometer in the 2θ range from 10° to 140° with a step size of 0.02°. Rietveld refinement was performed using TOPAS 5 software, specifics are given in the supplementary information (Table S1). The particle and electrode morphology were evaluated by SEM using a Zeiss Crossbeam 340 field-emission electron microscope equipped with an in-lens detector. The acceleration voltage was set to 3 kV.

The thermal stability of synthesized SPEs was evaluated by TGA (TG 209F1 Libra, Netzsch). SPE membranes were introduced in sealed Al pans and opened immediately before the measurement by the instrument. After a 30 min isothermal step at 30 °C, the samples were heated up to 600 °C with a heating rate of 5 K min^{-1} in an inert N_2 atmosphere. Thermal transitions were studied by DSC (Discovery DSC, TA Instruments) of samples hermetically sealed in Al pans. A 30 min isothermal equilibration step at 40 °C was followed by two cooling and heating cycles between −120 °C and 90 °C with a cooling/heating rate of 5 K min^{-1} and 30 min isothermal holds at the turning points. All DSC measurements were performed in duplicate. Glass transition temperatures (T_g) were determined by the midpoint method from all heating traces and averaged.

Cell Assembly and electrochemical characterization. The electrochemical stability of SPEs was evaluated in two-electrode sodium half-cells assembled in CR2032 coin-cells utilizing Al foil as working electrode and Na metal as counter and reference electrode. The Na metal (99.8 %, Across Organics) was cut, roll pressed, and punched into 13 mm diameter discs. SPE membranes with 16 mm diameter were punched out for the coin-cell configuration. LSV was performed to a lower limit of −2 V and an upper limit of 7 V vs. Na/Na^+ at a scan rate of 0.1 mV s^{-1} with a multi-channel potentiostat-galvanostat (VMP3, Biologic Science Instruments). Symmetric Cu/Cu blocking cells with a geometrical electrode area of 4 cm^2 were built in pouch-cell configuration to determine the temperature dependent conductivity of SPEs by EIS. A potentiostat-galvanostat (Solartron SI 1287, AMETEK) coupled with a frequency response analyzer (Solartron SI 1260, AMETEK) was used to apply an AC potential amplitude of 10 mV over the frequency range from 1 MHz to 1 Hz. For temperature control, the measurements were performed in a climatic chamber (Binder GmbH) and pouch-cells were allowed to equilibrate for 3 h after a temperature change. A representative impedance spectrum and the equivalent circuit used to fit the data are shown in Figure S9. To study the Na|SPE interface stability, EIS (AC potential amplitude of 10 mV, frequency range of 1 MHz to 0.1 Hz) was applied to symmetric Na|SPE|Na cells assembled in CR2032 coin-cells resting at OCV for 24 h employing a multi-channel potentiostat-galvanostat (VMP3, Biologic Science Instruments). This was followed by 10 cycles of 1 h stripping and 1 h plating with a current density of 26 μA cm^{-2} and EIS within a rest time of 1 h.

Sodium-metal polymer cells (Na|SPE|NM) were assembled in CR2032 coin-cells comprising 13 mm diameter sodium metal

anodes, SPE and NM cathodes. For comparison, cells utilizing non-aqueous liquid electrolytes, i.e., organic- and IL-based, soaked in glass fiber separators (Whatman, GF/D) instead of the SPE were assembled in three-electrode Swagelok® T-cells. As electrolyte solution, 1 M sodium hexafluorophosphate ($NaPF_6$, battery grade, FluoroChem) in propylene carbonate (PC, battery grade, UBE, Japan), and NaX in $Pyr_{14}X$ (X = FSI or TFSI, molar ratio of 1:4) were used, respectively. After a rest time of 2 h (liquid electrolyte) or 6 h (SPE), galvanostatic cycling of the cells within a voltage range of 3.8–1.5 V was performed by using a Maccor 4000 battery tester applying a constant current of 17 mA g^{-1} ($\approx$0.1 C, nominal capacity is 173 mAh g^{-1}, corresponding to $^2/_3$ equivalent of Na per mole of material). All electrochemical measurements were performed in climatic chambers (Binder GmbH) at 20 °C ± 2 °C, if not stated otherwise. To ensure good contact between the SPE and electrodes, a drop (20 µL) of salt/IL solution (molar ratio of 1:4) corresponding to the particular SPE was applied at the electrode|SPE interface. Because of porosity, the NM electrodes were subjected to a vacuum for 10 min after wetting. An exception is bare metal foil electrodes, i.e., the Cu/Cu blocking cells and the Al working electrode in cells subjected to LSV.

Supporting Information

The authors have cited additional references within the Supporting Information.[42]

Acknowledgements

The authors acknowledge the financial support from the BMBF TRANSITION project (FKZ 03XP0186 A) and the Helmholtz Association. Open Access funding enabled and organized by Projekt DEAL.

Conflict of Interests

The authors declare no conflict of interest.

Data Availability Statement

The data that support the findings of this study are available on request from the corresponding author. The data are not publicly available due to privacy or ethical restrictions.

[1] I. Hasa, S. Mariyappan, D. Saurel, P. Adelhelm, A. Y. Koposov, C. Masquelier, L. Croguennec, M. Casas-Cabanas, *J. Power Sources* **2021**, *482*, 228872.
[2] G. G. Eshetu, G. A. Elia, M. Armand, M. Forsyth, S. Komaba, T. Rojo, S. Passerini, *Adv. Energy Mater.* **2020**, *10*, 2000093.
[3] J. Yang, H. Zhang, Q. Zhou, H. Qu, T. Dong, M. Zhang, B. Tang, J. Zhang, G. Cui, *ACS Appl. Mater. Interfaces* **2019**, *11*, 17109.
[4] J. Janek, W. G. Zeier, *Nat. Energy* **2016**, *1*, 16141.
[5] a) S. Ohno, A. Banik, G. F. Dewald, M. A. Kraft, T. Krauskopf, N. Minafra, P. Till, M. Weiss, W. G. Zeier, *Prog. Energy Combust. Sci.* **2020**, *2*, 022001; b) Y. Kato, S. Hori, T. Saito, K. Suzuki, M. Hirayama, A. Mitsui, M. Yonemura, H. Iba, R. Kanno, *Nat. Energy* **2016**, *1*, 16030.
[6] a) A. Varzi, R. Raccichini, S. Passerini, B. Scrosati, *J. Mater. Chem. A* **2016**, *4*, 17251; b) C. Zhao, L. Liu, X. Qi, Y. Lu, F. Wu, J. Zhao, Y. Yu, Y.-S. Hu, L. Chen, *Adv. Energy Mater.* **2018**, *8*, 1703012; c) Q. Zhao, S. Stalin, C.-Z. Zhao, L. A. Archer, *Nat. Rev. Mater.* **2020**, *5*, 229.
[7] L. Qiao, X. Judez, T. Rojo, M. Armand, H. Zhang, *J. Electrochem. Soc.* **2020**, *167*, 070534.
[8] X. Qi, Q. Ma, L. Liu, Y.-S. Hu, H. Li, Z. Zhou, X. Huang, L. Chen, *ChemElectroChem* **2016**, *3*, 1741.
[9] J. Serra Moreno, M. Armand, M. B. Berman, S. G. Greenbaum, B. Scrosati, S. Panero, *J. Power Sources* **2014**, *248*, 695.
[10] A. Boschin, P. Johansson, *Electrochim. Acta* **2015**, *175*, 124.
[11] F. Croce, G. B. Appetecchi, L. Persi, B. Scrosati, *Nature* **1998**, *394*, 456.
[12] Y.-Q. Lyu, J. Yu, J. Wu, M. B. Effat, F. Ciucci, *J. Power Sources* **2019**, *416*, 21.
[13] J. Zhang, H. Wen, L. Yue, J. Chai, J. Ma, P. Hu, G. Ding, Q. Wang, Z. Liu, G. Cui, L. Chen, *Small* **2017**, *13*, 1601530.
[14] K. Pfeifer, S. Arnold, J. Becherer, C. Das, J. Maibach, H. Ehrenberg, S. Dsoke, *ChemSusChem* **2019**, *12*, 3312.
[15] a) M. Armand, F. Endres, D. R. MacFarlane, H. Ohno, B. Scrosati, *Nat. Mater.* **2009**, *8*, 621; b) I. Osada, H. de Vries, B. Scrosati, S. Passerini, *Angew. Chem. Int. Ed.* **2016**, *55*, 500.
[16] M. Watanabe, T. Mizumura, *Solid State Ionics* **1996**, *86–88*, 353.
[17] J.-H. Shin, W. A. Henderson, S. Passerini, *Electrochem. Commun.* **2003**, *5*, 1016.
[18] A. Boschin, P. Johansson, *Electrochim. Acta* **2016**, *211*, 1006.
[19] B. Rupp, M. Schmuck, A. Balducci, M. Winter, W. Kern, *Eur. Polym. J.* **2008**, *44*, 2986.
[20] M. A. A. Rani, J. Hwang, K. Matsumoto, R. Hagiwara, *J. Electrochem. Soc.* **2017**, *164*, H5031.
[21] A. Fdz De Anastro, N. Lago, C. Berlanga, M. Galcerán, M. Hilder, M. Forsyth, D. Mecerreyes, *J. Membr. Sci.* **2019**, *582*, 435.
[22] Y. Kim, M. Künzel, D. Steinle, X. Dong, G.-T. Kim, A. Varzi, S. Passerini, *Energy Environ. Sci.* **2022**, *15*, 2610.
[23] C. Wang, Y. S. Meng, K. Xu, *J. Electrochem. Soc.* **2019**, *166*, A5184.
[24] Z. W. Seh, J. Sun, Y. Sun, Y. Cui, *ACS Cent. Sci.* **2015**, *1*, 449–455.
[25] M. Xu, Y. Li, M. Ihsan-Ul-Haq, N. Mubarak, Z. Liu, J. Wu, Z. Luo, J. K. Kim, *Energy Storage Mater.* **2022**, *44*, 477–486.
[26] C. Zhu, D. Wu, Z. Wang, H. Wang, J. Liu, K. Guo, Q. Liu, J. Ma, *Adv. Funct. Mater.* **2023**, 2214195.
[27] H. de Vries, S. Jeong, S. Passerini, *RSC Adv.* **2015**, *5*, 13598.
[28] Z. Chen, D. Stepien, F. Wu, M. Zarrabeitia, H.-P. Liang, J.-K. Kim, G.-T. Kim, S. Passerini, *ChemSusChem* **2022**, *15*, e202200038.
[29] G. G. Eshetu, S. Grugeon, H. Kim, S. Jeong, L. Wu, G. Gachot, S. Laruelle, M. Armand, S. Passerini, *ChemSusChem* **2016**, *9*, 462.
[30] J. Huang, A. F. Hollenkamp, *J. Phys. Chem. C* **2010**, *114*, 21840.
[31] L. G. Chagas, S. Jeong, I. Hasa, S. Passerini, *ACS Appl. Mater. Interfaces* **2019**, *11*, 22278.
[32] D. T. Hallinan Jr., N. P. Balsara, *Annu. Rev. Mater. Res.* **2013**, *43*, 503.
[33] A. J. Bard, L. R. Faulkner, *Electrochemical Methods: Fundamentals and Applications*, John Wiley & Sons, Inc., New York **2001**.
[34] Z. Lu, J. R. Dahn, *J. Electrochem. Soc.* **2001**, *148*, A1225.
[35] M. H. Han, E. Gonzalo, G. Singh, T. Rojo, *Energy Environ. Sci.* **2015**, *8*, 81.
[36] D. H. Lee, J. Xu, Y. S. Meng, *Phys. Chem. Chem. Phys.* **2013**, *15*, 3304.
[37] a) L. G. Chagas, D. Buchholz, L. Wu, B. Vortmann, S. Passerini, *J. Power Sources* **2014**, *247*, 377; b) K. Wang, H. Zhuo, J. wang, F. Poon, X. Sun, B. Xiao, *Adv. Funct. Mater.* **2023**, 2212607.
[38] a) X. Judez, H. Zhang, C. Li, J. A. González-Marcos, Z. Zhou, M. Armand, L. M. Rodriguez-Martinez, *J. Phys. Chem. Lett.* **2017**, *8*, 1956; b) L. Qiao, A. Santiago, Y. Zhang, M. Martinez-Ibañez, E. Sanchez-Diez, E. Lobato, M. Treskow, P. Johansson, H. Zhang, M. Armand, *J. Electrochem. Soc.* **2020**, *167*, 120541.
[39] I. Hasa, D. Buchholz, S. Passerini, J. Hassoun, *ACS Appl. Mater. Interfaces* **2015**, *7*, 5206.
[40] Z. Chen, G.-T. Kim, Z. Wang, D. Bresser, B. Qin, D. Geiger, U. Kaiser, X. Wang, Z. X. Shen, S. Passerini, *Nano Energy* **2019**, *64*, 103986.
[41] M. Montanino, F. Alessandrini, S. Passerini, G. B. Appetecchi, *Electrochim. Acta* **2013**, *96*, 124.
[42] a) Z. Li, Y. Zhao, W. E. Tenhaeff, *Chem. Mater.* **2021**, *33*, 1927; b) Y. Xia, T. Fujieda, K. Tatsumi, P. P. Prosini, T. Sakai, *J. Power Sources* **2001**, *92*, 234.

Manuscript received: March 9, 2023
Revised manuscript received: May 23, 2023
Accepted manuscript online: May 25, 2023
Version of record online: June 14, 2023